

Animating Vital Signs in Radar Simulations: Comparing Physical Optics Against 28.5 GHz Channel Measurements

Swagato Mukherjee*, Benjamin M. Hardy*, Greg J. Skidmore*, Tarun Chawla*, Jihoon Bang†‡, Jack Chuang§, Jelena Senic†‡, Samuel Berweger†, Steve Blandino§¶, Camillo Gentile§

*Remcom Inc., State College, PA USA

†Communications Technology Lab, NIST, Boulder CO, USA

‡Department of Physics, University of Colorado Boulder, Boulder, Colorado, USA

§Communications Technology Lab, NIST, Gaithersburg, MD, USA

¶Prometheus Computing LLC, Bethesda, MD, USA

Corresponding author: swagato.mukherjee@remcom.com

Abstract—Monitoring vital signs such as breathing or heart rates as well as other physical movements in complex environments is the basis for many emerging applications spanning from healthcare to autonomous vehicles. Designing Radar systems capable of remotely monitoring these movements necessitates measurement campaigns in combination with advanced machine-learning algorithms. Despite the compelling applications and the need for large and diverse data sets for validation of design, there are few examples of simulated human movement in multipath environments in the literature. To address this gap, the work presented here outlines a method to accurately simulate Radar back-scatter from time varying human movement. Specifically, we animate human breathing with anatomically accurate mathematical models through physical-optics-based simulation and validated them against monostatic Radar measurements with a 28.5 GHz channel sounder in a semi-anechoic chamber by the National Institute of Standards and Technology, capturing phase and path loss over time from a human breathing positioned 2 m away. Using vital sensor data as ground truth, we demonstrate the animations to match the simulated human’s breathing patterns and heart rate. Furthermore, the simulation resulted in excellent agreement with the measured phase across ten breaths, and had a root-mean-square error (RMSE) of 2.1 dB in path loss.

Index Terms—Raytracing, Physical Optics, human breathing, mmWave, WaveFarer

I. INTRODUCTION

Radar-based non-contact vital sign (NCVS) monitoring systems have a wide range of application across industries [1]–[3]. The techniques have been thoroughly demonstrated in research settings, the clinic, and marketplace products. In medicine, radar methods minimize contact with patients while avoiding the privacy concerns of camera-based monitoring [4]. Respiration and heart beat have been measured in clinical trials using 2.4 GHz radar [2], [5]. Furthermore, advanced heart sound monitoring has been demonstrated using 24.1 GHz radar combined with advanced algorithms [6]. Other medical applications of radar-based monitoring include sleep disorder diagnosis [7], fall detection [8], and palliative care [9].

Outside of biomedical applications, there is increasing demonstration of highly accurate feature detection using radar

micro-doppler [10] such as distinguishing birds from drones [11] and hand gesture recognition [12]. Similarly, sensing is becoming more integrated in highly connected “smart” homes equipped with radar security systems or cars with advanced driver assistance systems [13]–[15]. For radar sensing and micro-doppler applications, the complex back-scattering from reflected and refracted signals is often fed into intelligent algorithms such as k-nearest neighbor algorithms [12], machine learning (ML) [16], or neural networks (NN) [17].

For ML or NN based systems there is a need for large training data sets from lengthy measurement campaigns or physics informed data sets. Simulation tools offer a great alternative to in situ measurement in speed, scalability, and customization. However, examples of validated computer modeling that accurately capture radar fading, back-scattering, and micro-doppler of vital signs or gestures are limited. Simulation of the radar cross section (RCS) of a humanoid using physical optics (PO) has been previously achieved [18], however the humanoid was static and the study focused on the validity of the methods presented.

Numerical electromagnetic solvers based on ray-tracing methods may use PO to accurately simulate back-scattering problems. In this article, we utilize the PO solver available in Remcom’s *WaveFarer*® radar simulation tool [19]¹ to simulate back-scatter from the chest of an animated human model and compare the predictions against 28.5 GHz measurements collected by the National Institute of Standards and Technology (NIST). The novelty of this work is twofold:

- 1) It presents a method to accurately animate vital signs over time in simulation.
- 2) It simulates multipath components over time including back-scattering and fading validated with measurements.

¹Certain equipment, instruments, software, or materials are identified in this paper in order to specify the experimental procedure adequately. Such identification is not intended to imply recommendation or endorsement of any product or service by NIST, nor is it intended to imply that the materials or equipment identified are necessarily the best available for the purpose.

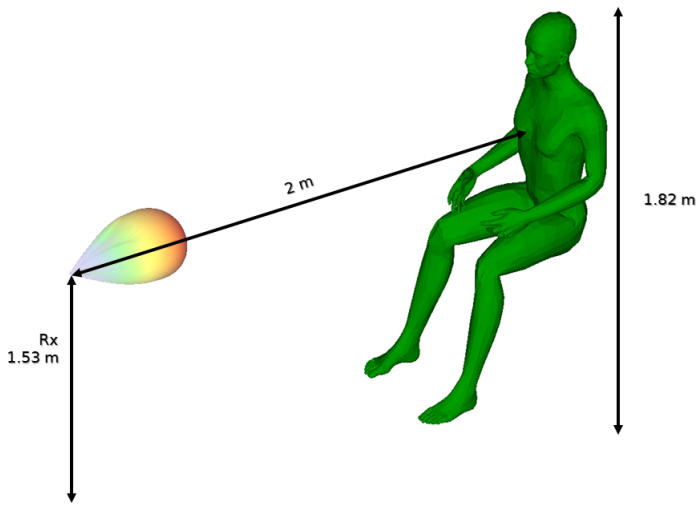


Fig. 1. The human subject's dimensions and relative positioning with respect to the Rx for the measurement campaign and simulation. The center of the Rx was 1.53 m from the ground, the human chest 2 m from the Rx, and the top of the head 1.82 m from the ground.

II. METHODS

A. Measurement Methods (NIST)

1) *Measurement Setup*: The measurements performed at NIST utilized a single dual-polarized phased-array board of 64 microstrip antennas at the transmitter (Tx), and four of the same boards stacked side-by-side (256 microstrip antennas) at the receiver (Rx), a 360° azimuth camera, lidar and *Movesense* vital sensors. The antenna array channel and sounding technique were previously described in [20]. For the measurements described in this article a human sat 2 m from the Rx. Relative positioning of the subject to the Rx is described in Fig. 1 and Table I. Samples were collected every 26 ms with the subject breathing at a normal rate for 25 s while vital signs were monitored.

TABLE I
SUBJECT POSITIONING

Feature	Elevation angle (°)	height (m)
Head (nose)	7.7	1.8
Shoulder	2.6	1.71
Chest	0	1.53, 0.37 ^a
Stomach	-3.7	1.4

^aWidth of shoulders.

2) *Path loss and Phase from Measured Data*: The measurement data comprised of time of arrival (ToA), angle-of-arrival (AoA) in the elevation and azimuth planes, path loss, and phase for each multipath component (MPC). Assuming 0 dBm Tx power, the normalized received power (P_i) for the i th MPC can then be defined as,

$$P_i = 10^{(-PL_i/10)} \quad (1)$$

where, PL_i is the path loss per MPC. A ToA- and AoA-based search method is used to identify the MPCs that back-

scatter from the human subject. The normalized received power and phase for these MPCs are combined to obtain the total normalized received power (P) as,

$$P = \left| \sum_{i=1}^N \sqrt{P_i} \exp(j\phi_i) \right|^2 \quad (2)$$

where N is the number of selected MPCs, and ϕ_i is the phase of i^{th} component. The total received phase may be described as

$$\Phi = \angle \sum_{i=1}^N \sqrt{P_i} \exp(j\phi_i) \quad (3)$$

The total path loss (PL) is then defined as,

$$PL = -10 \log_{10}(P). \quad (4)$$

B. Simulation Methods

1) *EM Prediction using Physical Optics*: To accurately simulate the back-scatter observed in the measurements we utilised a 3D human phantom, as shown in Fig. 1. The human phantom surface has 8210 facets, each of which is associated with different radii of curvature. Scattering from the complex surface is precisely modeled by PO [21], as it performs a surface integral that incorporates the sizes and shapes of small facets on the surface.

In the PO method, the scattered field is computed from the surface currents on the scattering object due to the incident geometric optics (GO) fields. The scattered far-fields are then obtained from these surface currents by performing the radiation integrals. The scattered field computation can be mathematically expressed through vector potentials [22] given by

$$\mathbf{A} = \frac{\mu}{4\pi} \iint_S \mathbf{J}_S \frac{e^{-jkR}}{R} dS' \quad (5)$$

$$\mathbf{F} = \frac{\epsilon}{4\pi} \iint_S \mathbf{M}_S \frac{e^{-jkR}}{R} dS' \quad (6)$$

where \mathbf{A} is the far-field magnetic vector potential, μ is the magnetic permeability, \mathbf{J}_S is the surface electric current density, R is the radial distance between the source and the observation point, S is the integration surface, \mathbf{F} is the far-field electric vector potential, ϵ is the electric permittivity, and \mathbf{M}_S is the surface magnetic current density. Consequently, the scattered far-field electric (E_{scat}) and magnetic (H_{scat}) fields are given by,

$$E_{scat} \approx -j\omega\mathbf{A} - \frac{1}{\epsilon} \nabla \times \mathbf{F} \quad (7)$$

$$H_{scat} \approx -j\omega\mathbf{F} + \frac{1}{\mu} \nabla \times \mathbf{A} \quad (8)$$

where ω is the angular frequency of the scattered wave. The GO surface currents do not capture the non-uniformity of the current densities close to an edge, thus the method of equivalent currents [19] must be used to add the effects of edge diffraction to the PO scattered field solution. In this study, we used *WaveFarer's* PO solver to simulate the back-scatter from the human phantom.

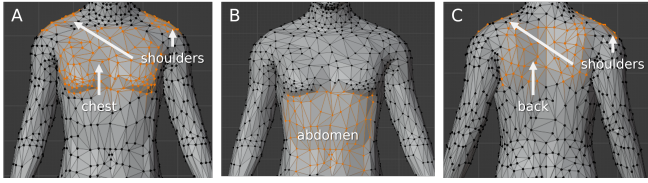


Fig. 2. The animated vertices are highlighted in orange. *A* shows the vertices representing the shoulders and chest. *B* shows the abdomen. *C* shows the back and shoulder vertices.

2) *Animations in Blender*: In order to accurately capture small changes in the human phantom due to breathing and the heart beating, animations were mathematically modelled using the open source 3D creation suite, *Blender 3.5.1*. The human model is surface based with 4122 vertices and 8210 facets. Animations were performed by manually selecting vertices on the chest, shoulders, back, and abdomen to localize displacement due to breathing and the heart beating. The vertices selected on the human model can be seen in Fig. 2.

The vertices' displacement over time due to the lungs inhaling and exhaling air follows the equations given by [23]. The chest, shoulders, abdomen, and back are animated over time using

$$r_{breath}(t) = \begin{cases} \frac{-r_{max}}{T_i T_e} t^2 + \frac{r_{max} T}{T_i T_e} t & t \leq T_i \\ \frac{r_{max}}{1 - e^{-T_e/\tau}} (e^{-(t - T_e)/\tau} - e^{-T_e/\tau}) & T_i < t \leq T \end{cases} \quad (9)$$

where r_{max} is the maximum displacement due to a breath, T_i the inspiration time, T_e the expiration time, T is the time period of one breath where $T = T_e + T_i$, and τ is the decay constant of the expiration. The displacement due to the heart beating was modelled with a simple sinusoid as

$$r_{heart}(t) = r_{h,max} \sin(2\pi t HR/60) \quad (10)$$

where $r_{h,max}$ is the maximum displacement due to the heart and HR is the heart rate in beats per minute (bpm). The total displacement on the chest where the heart and breathing contribute to movement was animated over time as

$$r_{total}(t) = r_{breath}(t) + r_{heart}(t) \quad (11)$$

Figure 3 demonstrates the contributions of Eqs. (9), (10), and (11).

Using *Blender's* python scripting interface, each set of vertices is associated with a shape key. When the shape key is fully activated, the r_{max} is applied to each group of vertices. The shape key is then linked to expressions outlined in Eq. (9) and Eq. (10) where all time variables are converted to units of frames where one frame is arbitrarily chosen to last 1 ms. As the frames change, the magnitude of the shape key and thus the displacement of the vectors is adjusted following the expressions. Key frames of animation are exported as .STL files at variable sample rates. The .STL file export was set to every 50 frames (50 ms sample rate) to minimize the number of simulation runs. Following [23], T_i/T_e was assumed to be 0.6 and τ was set to $T_e/5$. The remaining parameters:

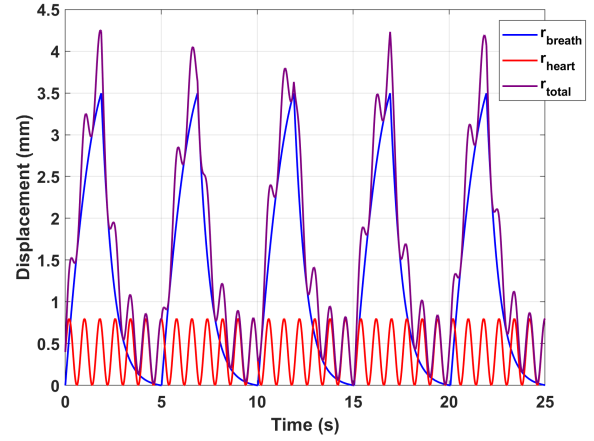


Fig. 3. Mathematical model of displacement due to breathing, the heart beat, and their combined sum. The data represent 12 breaths/min, $T_e = 3.125$ s, $T_i = 1.875$ s, $\tau = T_e/5$, $HR = 75$ bpm, and 3.5 and 0.8 mm for the maximum displacement for the breathing and heart respectively.

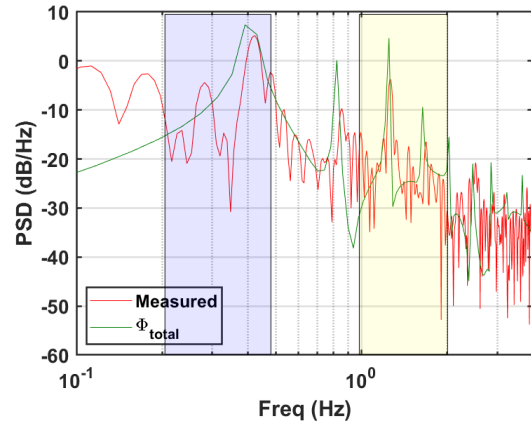


Fig. 4. Power spectral density of Φ (Measured) and Φ_{total} . The blue box in the image denotes the frequency components of interest due to breathing alone (12 breaths/min to 30 breaths/min); while the yellow box denotes the same for heartbeat (60 bpm to 120 bpm).

(r_{max} , $r_{h,max}$, HR , and breath rate) were estimated from the measurement campaign described in section II-C.

C. Parameter Extraction from Measured Data

In order for the animation to accurately represent the human breathing, some parameters were extracted from the measurements. The vital monitors electrocardiogram (ECG) data reported the heart rate as 75 bpm. r_{max} , $r_{h,max}$, and the breath rate were not measured directly but were estimated from the fluctuations in the total received phase. The power spectral density (PSD) of the total received phase Φ , is plotted in Fig. 4 (red solid line). Normal human breathing rates at rest fall between 12 breaths/min to 30 breaths/min and are indicated by the blue box in Fig. 4. Similarly, the yellow box in Fig. 4 denotes the frequency range of interest due to the heart beating at a resting normal rate (i.e. 60-120 bpm). The peak in the breathing region corresponds to a breathing rate

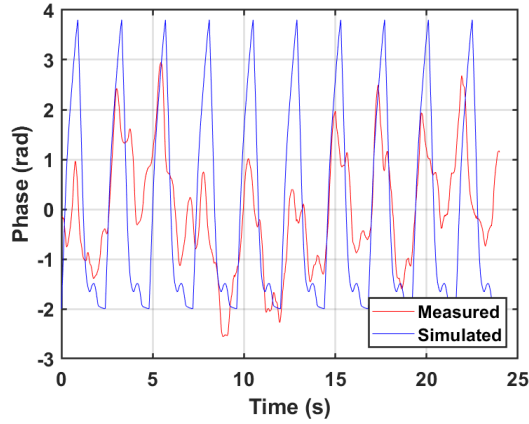


Fig. 5. Comparison of simulated phase to measured phase.

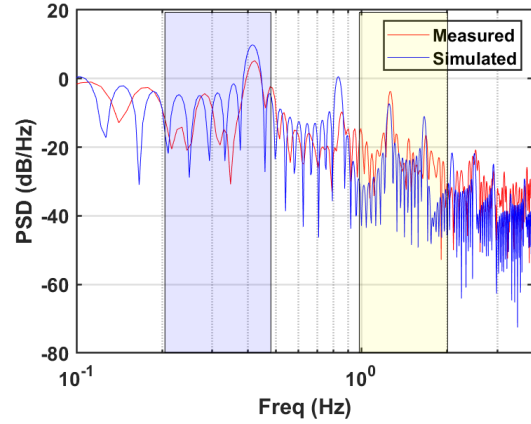


Fig. 6. Comparison of simulated PSD to measured PSD.

of ≈ 25 breaths/min (0.42 Hz). The heartbeat region shows the dominant heartbeat frequency as 75 bpm (1.25 Hz) which matched the ECG data.

Next, the maximum chest displacement due to breathing, r_{max} , was estimated from the peak power in the breathing region as 3.5 mm. Since the dominant heartbeat frequency coincided with the third harmonic due to breathing, it is not possible to directly predict the $r_{h,max}$ from the PSD of the measured phase alone. Hence, the phase shift due to r_{total}

$$\Phi_{total} = \frac{2\pi r_{total}}{\lambda} \quad (12)$$

was defined, where λ is the signal wavelength. Φ_{total} 's PSD was plotted against the measurement as shown by the solid green line in Fig. 4. By comparing the two PSDs, it was found that $r_{h,max} = 0.8$ mm provided the best match of the power level at 1.25 Hz.

III. COMPARISON OF SIMULATED AND MEASURED PATH LOSS AND PHASE

Blender-generated breathing animation with the human phantom was imported as snapshots every 50 ms into *WaveFarer*. The human phantom was assigned a skin relative permittivity of $\epsilon_r = 15.5 - 14.2j$, as reported for 28 GHz in [24]. The Tx and Rx were assigned Gaussian antenna patterns with 22.5° half-power bandwidth (HPBW) in the elevation and 30° HPBW in the azimuth plane. Both the Tx and Rx were located at the same location and 2 m away from the human phantom. The polarization was vertical for Rx and Tx. Each simulation in *WaveFarer* with the PO model took approximately 2 min. The simulation was run for one breath period (2.4 s) and the path loss and phase simulated during that one period was concatenated to compare against the 10 breaths that were measured.

First, we compare the simulated and measured phase in Fig. 5 and their PSDs in Fig. 6. Excellent agreement between the phase and the PSD show that we have accurately predicted the breathing and heartbeat parameters, and have established a successful process to generate realistic simulations through

Blender animations imported in *WaveFarer*. Variations between the measurement and simulation in Fig. 5 may be due to the breathing rate varying over time, the heart rate's phase varying each breath, and each breath varying in maximum displacement. It is also possible that the subject slightly moves towards (breath 3) or away (breath 4) from the Rx.

Next, the measured and simulated path loss are compared in Fig. 7. The path loss shows good agreement with a root-mean-squared error (RMSE) of 2.1 dB across the 10 breaths. Note that the RMSE is defined as,

$$RMSE = \sqrt{\frac{1}{N} \sum_{n=1}^N (PL_{meas}^n - PL_{sim}^n)^2} \quad (13)$$

where PL_{meas}^n and PL_{sim}^n are respectively the measured and simulated path loss in dB at time index n , and N is the total number of measurements. The simulation data set was interpolated to match the measured data since the measurement was performed every 26 ms versus every 50 ms for the simulations. The simulations overestimate the path loss slightly. This may be due to the neglect of the effect of clothing, and the physical differences between the simulated human phantom and the person whose breathing was measured.

IV. CONCLUSION

In this study, we demonstrate a process to realistically animate a human phantom through the open-source software *Blender* and import those animations into the *WaveFarer* radar simulation tool to simulate back-scatter from the human chest due to breathing and the heart beat. The PO method in *WaveFarer* yielded a RMSE of 2.1 dB when compared against 28.5 GHz measurements provided by NIST. Excellent match in received phase was also shown.

Future work will include study of back-scatter from other human postures like standing and lying down with the inclusion of more realistic human movements where breathing rate, heart rate, and their displacement amplitudes vary across time. *WaveFarer* simulations will sweep parameters for improved agreement between measurement and simulation. Additional

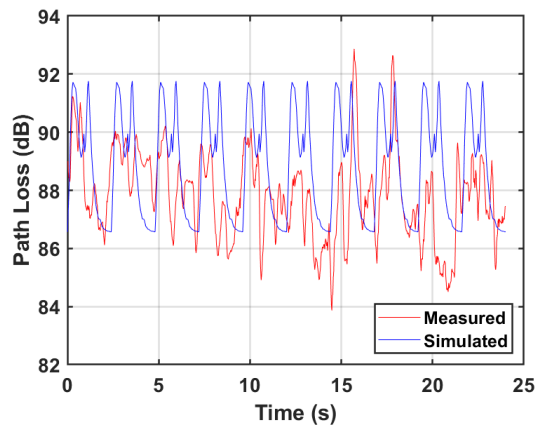


Fig. 7. Comparison of simulated path loss to measured path loss.

noise sources such as clothing will be investigated by the inclusion of a surface roughness factor in *WaveFarer*.

ACKNOWLEDGMENT

The authors would like to thank Sam Magliaro and Walter Janusz at Remcom for their help with the human phantom animation process.

REFERENCES

- [1] C. G. Caro and J. A. Bloice, "Contactless apnoea detector based on radar," *Lancet (London, England)*, vol. 2, pp. 959–961, 10 1971. [Online]. Available: <https://pubmed.ncbi.nlm.nih.gov/4107906/>
- [2] Y. Liu, C. Sweeney, J. C. Mayeda, J. Lopez, P. E. Lie, T. Q. Nguyen, and D. Y. C. Lie, "A feasibility study of remote non-contact vital signs (NCVS) monitoring in a clinic using a novel sensor realized by software-defined radio (SDR)," *Biosensors*, vol. 13, no. 2, 2023. [Online]. Available: <https://www.mdpi.com/2079-6374/13/2/191>
- [3] C. Li, V. M. Lubecke, O. Boric-Lubecke, and J. Lin, "A review on recent advances in doppler radar sensors for noncontact healthcare monitoring," *IEEE Transactions on Microwave Theory and Techniques*, vol. 61, no. 5, pp. 2046–2060, 2013.
- [4] S. M. M. Islam, "Radar-based remote physiological sensing: Progress, challenges, and opportunities," *Frontiers in Physiology*, vol. 13, 2022. [Online]. Available: <https://www.frontiersin.org/articles/10.3389/fphys.2022.955208>
- [5] T. Hall, D. Y. C. Lie, T. Q. Nguyen, J. C. Mayeda, P. E. Lie, J. Lopez, and R. E. Banister, "Non-contact sensor for long-term continuous vital signs monitoring: A review on intelligent phased-array doppler sensor design," *Sensors*, vol. 17, no. 11, 2017. [Online]. Available: <https://www.mdpi.com/1424-8220/17/11/2632>
- [6] C. Will, K. Shi, S. Schellenberger, T. Steigleder, F. Michler, J. Fuchs, R. Weigel, C. Ostgathe, and A. Koelpin, "Radar-based heart sound detection," *Scientific Reports*, vol. 8, p. 11551, 2018. [Online]. Available: <https://doi.org/10.1038/s41598-018-29984-5>
- [7] S. Kang, Y. Lee, Y.-H. Lim, H.-K. Park, S. H. Cho, and S. H. Cho, "Validation of noncontact cardiorespiratory monitoring using impulse-radio ultra-wideband radar against nocturnal polysomnography," *Sleep and Breathing*, vol. 24, pp. 841–848, 2020. [Online]. Available: <https://doi.org/10.1007/s11325-019-01908-1>
- [8] A. Bhattacharya and R. Vaughan, "Deep learning radar design for breathing and fall detection," *IEEE Sensors Journal*, vol. 20, no. 9, pp. 5072–5085, 2020.
- [9] K. Shi, C. Will, T. Steigleder, F. Michler, R. Weigel, C. Ostgathe, and A. Koelpin, "A contactless system for continuous vital sign monitoring in palliative and intensive care," in *2018 Annual IEEE International Systems Conference (SysCon)*, 2018, pp. 1–8.
- [10] V. Chen, F. Li, S.-S. Ho, and H. Wechsler, "Micro-doppler effect in radar: phenomenon, model, and simulation study," *IEEE Transactions on Aerospace and Electronic Systems*, vol. 42, no. 1, pp. 2–21, 2006.

- [11] S. Rahman and D. A. Robertson, "Radar micro-doppler signatures of drones and birds at K-band and W-band," *Scientific Reports* 2018 8:1, vol. 8, pp. 1–11, 11 2018. [Online]. Available: <https://www.nature.com/articles/s41598-018-35880-9>
- [12] M. G. Amin, Z. Zeng, and T. Shan, "Hand gesture recognition based on radar micro-doppler signature envelopes," in *2019 IEEE Radar Conference (RadarConf)*, 2019, pp. 1–6.
- [13] S. Ahmed, K. D. Kallu, S. Ahmed, and S. H. Cho, "Hand gestures recognition using radar sensors for human-computer-interaction: A review," *Remote Sensing*, vol. 13, no. 3, 2021. [Online]. Available: <https://www.mdpi.com/2072-4292/13/3/527>
- [14] J.-K. Park, Y. Hong, H. Lee, C. Jang, G.-H. Yun, H.-J. Lee, and J.-G. Yook, "Noncontact RF vital sign sensor for continuous monitoring of driver status," *IEEE Transactions on Biomedical Circuits and Systems*, vol. 13, no. 3, pp. 493–502, 2019.
- [15] G. Skidmore, T. Chawla, and G. Bedrosian, "Combining physical optics and method of equivalent currents to create unique near-field propagation and scattering technique for automotive radar applications," in *2019 IEEE International Conference on Microwaves, Antennas, Communications and Electronic Systems (COMCAS)*, 2019, pp. 1–6.
- [16] A. K. Alhazmi, M. A. Alanazi, C. Liu, and V. P. Chodavarapu, "Machine learning enabled fall detection with compact millimeter wave system," in *NAECON 2021 - IEEE National Aerospace and Electronics Conference*, 2021, pp. 217–222.
- [17] X. Huang, N. Patel, and K. P. Tsoi, "Application of mmwave radar sensor for people identification and classification," *Sensors*, vol. 23, no. 8, 2023. [Online]. Available: <https://www.mdpi.com/1424-8220/23/8/3873>
- [18] G. Manfredi, P. Russo, A. D. Leo, and G. Cerri, "Efficient simulation tool to characterize the radar cross section of a pedestrian in near field," *Progress in Electromagnetics Research C*, vol. 100, pp. 145–159, 2020. [Online]. Available: <https://api.semanticscholar.org/CorpusID:216519843>
- [19] *WaveFarer Reference Manual, Release 2.1.0, Remcom, Nov. 2020*.
- [20] D. Caudill, J. Chuang, S. Y. Jun, C. Gentile, and N. Golmie, "Real-time mmwave channel sounding through switched beamforming with 3D dual-polarized phased-array antennas," *IEEE Transactions on Microwave Theory and Techniques*, vol. 69, pp. 5021–5032, 11 2021.
- [21] S. Mukherjee, G. Skidmore, T. Chawla, A. Bhardwaj, C. Gentile, and J. Senic, "Scalable modeling of human blockage at millimeter-wave: A comparative analysis of knife-edge diffraction, the uniform theory of diffraction, and physical optics against 60 GHz channel measurements," *IEEE Access*, vol. 10, pp. 133 643–133 654, 2022.
- [22] C. A. Balanis, *Advanced Engineering Electromagnetics*. John Wiley & Sons, Inc, 2012.
- [23] A. Albanese, L. Cheng, M. Ursino, and N. W. Chbat, "An integrated mathematical model of the human cardiopulmonary system: model development," *American Journal of Physiology-Heart and Circulatory Physiology*, vol. 310, no. 7, pp. H899–H921, 2016, pMID: 26683899. [Online]. Available: <https://doi.org/10.1152/ajpheart.00230.2014>
- [24] T. Wu, T. S. Rappaport, and C. M. Collins, "The human body and millimeter-wave wireless communication systems: Interactions and implications," *IEEE International Conference on Communications (ICC)*, 2015.